Nanoscale Horizons

ROYAL SOCIETY OF CHEMISTRY

COMMUNICATION

View Article Online
View Journal | View Issue

Cite this: *Nanoscale Horiz.*, 2024, 9, 148

Received 16th June 2023,
Accepted 19th October 2023

DOI: 10.1039/d3nh00249g

rsc.li/nanoscale-horizons

Two-gap topological superconductor LaB_2 with high T_c = 30 K†

Chin-Hsuan Chen,‡[a] Ye-Shun Lan,‡[a] Angus Huang[a] and Horng-Tay Jeng *[abc]

Since two gap superconductivity was discovered in MgB_2, research on multigap superconductors has attracted increasing attention because of its intriguing fundamental physics. In MgB_2, the Mg atom donates two electrons to the borophene layer, resulting in a stronger gap from the σ band and a weaker gap from the π bond. First-principles calculations demonstrate that the two gap anisotropic superconductivity strongly enhances the transition temperature of MgB_2 in comparison with that given by the isotropic model. In this work, we report a three-band (B-σ, B-π, and La-d) two-gap superconductor LaB_2 with very high T_c = 30 K by solving the fully anisotropic Migdal–Eliashberg equation. Because of the σ and π–d hybridization on the Fermi surface, the electron–phonon coupling constant λ = 1.5 is significantly larger than the λ = 0.7 of MgB_2. Our work paves a new route to enhance the electron–phonon coupling strength of multigap superconductors with d orbitals. On the other hand, our $\mathbb{Z}_2$ analysis reveals that LaB_2 belongs to the weak topological semimetal category, leading to a possible topological superconductor with the highest T_c to date. Moreover, upon applying pressure and/or doping, the topology is tunable between weak and strong with T_c varying from 15 to 30 K, opening up a flexible platform for manipulating topological superconductors.

New concepts

To date, available topological superconductors such as $PbTaSe_2$, PdBi, $RhPb_2$, as well as WS_2 and SnPbTe/Pb heterostructures all belong to S-wave single-gap BCS superconductors. In our work, we present a two-gap topological superconductor LaB_2, which is a totally new concept to this field. Therefore, the impact to the topological superconductor, Majorana fermion, and quantum computing research fields will be strong. So far, available candidates such as $PbTaSe_2$, PdBi, $RhPb_2$, as well as WS_2 and SnPbTe/Pb heterostructures published in high-impact journals in recent years all have T_c below 10 K. Such a low T_c causes tremendous difficulties for accurately measuring the possible Majorana fermions experimentally. Thus, it is of great importance to discover high-T_c topological superconductors. In this work, we report a record-breaking high T_c of 30 K in the topological superconductor LaB_2, comparing highly favorably over all the available candidates.

Introduction

Superconductivity is one of the most important and mysterious research fields not only because of the intriguing fundamental physics behind it but also because of its high potential for future industry. Yet the critical temperature T_c of superconductors is generally too low for practical applications. Thus enhancing the T_c of superconductors is an essential issue in condensed matter physics. One successful approach to raise T_c is by applying pressure. In recent years, nearly room temperature T_c have been found in hydrogen-rich hydrides under high pressure such as H_3S,[1] LaH_{10},[2] and NaH_6.[3,4] The other approach to enhance the T_c of superconductors is through the anisotropic pairing or multigap mechanism such as in conventional superconductor magnesium diboride MgB_2.[5,6] In particular, the anisotropic pairing of unconventional superconductors, with the Cooper pairing different from the conventional s-wave pairing, has attracted extensive attention because of the many-body interactions among d-electrons in cuprate[7–10] and iron-based superconductors.[11,12] On the other hand, topological superconductors with p-wave pairing have also been predicted in Sr_2RuO_4.[13]

MgB_2, known as a classic example of an anisotropic pairing superconductor, has shown great promise for enhancing T_c through two-gap phonon-mediated superconductivity. The Fermi surfaces (FSs) of MgB_2 comprise σ bonds (s + $p_{x,y}$ orbitals of B atoms) and π bonds (p_z orbitals of B atoms).[5,14–19] The two separated FSs in reciprocal space lead to two superconducting (SC) gaps $\Delta_\sigma \approx 7$ meV and $\Delta_\pi \approx$ 2–3 meV at 0 K[20–23] with the gaps closed at the transition temperature T_c = 39 K.[20–23] Theoretical investigations demonstrate that the anisotropic effect increases the superconducting temperature of MgB_2 from

[a] *Department of Physics, National Tsing Hua University, Hsinchu 30013, Taiwan*
[b] *Physics Division, National Center for Theoretical Sciences, Taipei 10617, Taiwan*
[c] *Institute of Physics, Academia Sinica, Taipei 11529, Taiwan.*
E-mail: jeng@phys.nthu.edu.tw

† Electronic supplementary information (ESI) available. See DOI: https://doi.org/10.1039/d3nh00249g

‡ These authors contributed equally to this work.

19 K to 55 K in the harmonic approximation. Additionally, the anharmonicity increases the phonon energy of the E_{2g} mode at the Gamma point from 62.7 meV to 75.9 meV and decreases the total EPC strength from $\lambda = 0.73$ to $\lambda = 0.61$. Consequently, T_c decreases from 55 K to 39 K,[6] being in good consistence with the experimental T_c. The two-gap behavior exhibits exotic properties such as giant-paramagnetic response,[24] skyrmionic states,[25,26] hidden criticality,[27,28] and time-reversal symmetry breaking.[29,30]

In addition to bulk MgB_2, several systems have been proposed to exhibit multigap superconductivity. For example, two to three SC gaps with the transition-temperatures $T_c = 20$ K, 70 K, and 34.5 K were reported in monolayer of MgB_2, CaB_2, and ScB_2.[31,32] The trilayers of CaB_4, GaB_4, BeB_4 and LiB_4 films have multigaps with T_c of 64 K, 51 K, 39 K and 32 K, respectively.[32,33] Four SC gaps with a $T_c = 52$ K were predicted in trilayer system MgB_4 above bulk MgB_2.[33] Other than the magnesium boride family, multiband superconductivity has also been predicted in the hole doped LiBC with $T_c = 100$ K,[34] bulk AlB_2 with $T_c = 9$ K,[16,35] and thin film AlB_2 with T_c = 17–26.5 K.[16,35] These predictions show that the honeycomb layer structure with sp_2 hybridized orbitals is essential for finding multigap superconductivity. To date, bulk MgB_2 has been confirmed as a two-gap superconductor,[36] while the other predicted multigap phonon-mediated systems are yet to be confirmed in future experiments.

In this work, we investigate the superconductivity in the LaB_2 compound in the same crystal structure as MgB_2 through first-principles calculations. The superconducting critical temperature $T_c^{McMillan} = 22$ K is obtained for LaB_2 *via* the Allen–Dynes modified McMillan formula, while two-gap superconductivity with a notably higher $T_c^{aniso} = 30$ K is obtained through solving the fully anisotropic Migdal–Eliashberg equations. In addition, our $\mathbb{Z}_2$ analysis reveals LaB_2 to be a weak topological superconductor with the highest T_c in comparison with available candidates. The topology is tunable between weak and strong with superconducting T_c varying from 15 to 30 K upon applying pressure and/or doping, serving as a flexible candidate for topological superconductors.

Results and discussion

It is well known that magnesium diboride MgB_2 exhibits two-gap superconductivity with the highest ambient-pressure T_c to date. By substituting the magnesium atom with transition-metal elements, we systematically investigated the superconductivity of the transition-metal diboride XB_2. Among them, we found that LaB_2 can be stabilized in the same crystal structure as MgB_2 under ambient pressure, while it also shows two-gap superconductivity with a fairly high T_c of 30 K. LaB_2 is composed of alternate honeycomb boron and metallic lanthanum layers. The crystal structure with space group *P6/mmm* is shown in Fig. 1(a) and (b). The optimized lattice parameters a = 3.32 Å and c/a = 1.30 are obtained from geometry relaxation calculations based on density functional theory (DFT).

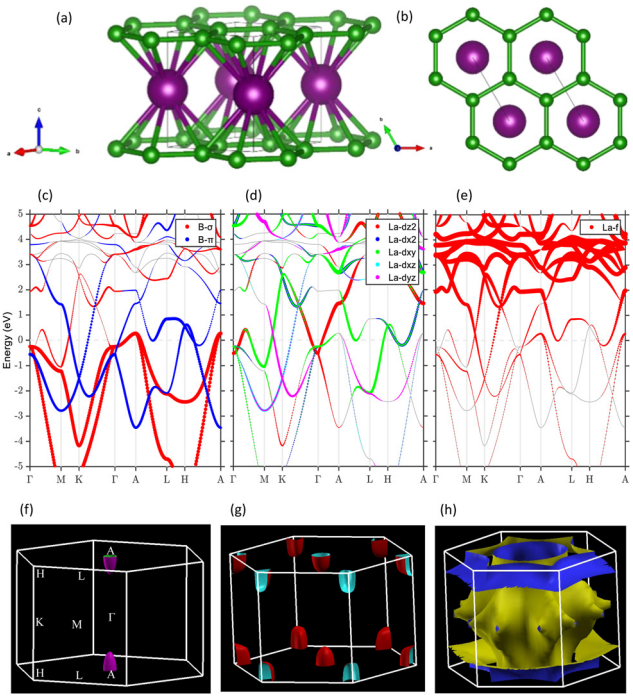

Fig. 1 LaB_2 hexagonal crystal structure and electronic properties. (a) Side view and (b) top view of the LaB_2 lattice structure. (c)–(e) Electronic band structure of LaB_2 projected onto the B-σ and B-π, La-d, and La-f orbital, respectively. The size of the colored spheres indicates the contributions from the atomic orbitals. (f)–(g) The Fermi surface near the *H* and *A* points is dominated by the boron π bond and boron σ bond, respectively. (h) The Fermi surface is dominated by the lanthanum d bond.

The atom-orbital-decomposed band structures depicted in Fig. 1(c)–(e) show the detailed characters of each electronic band. Near the Fermi level (E_F), the doubly degenerate boron-σ bands cross E_F from Γ to *A*, forming a small hole pocket around *A* (Fig. 1(c)). Similar to MgB_2, this slowly rising flat B-σ (sp^2) band along Γ–*A* reflects weak interlayer interactions in LaB_2 with a slightly higher E_F due to the relatively higher ionicity of La. One boron-π (p_z) band also crosses E_F and forms a hole pocket around *H* (Fig. 1(c)). On the other hand, the contributions of lanthanum (La) to the electronic bands plotted in Fig. 1(d and e) demonstrate that three La-d orbitals: d_{z^2}, $d_{x^2-y^2}$, and d_{xy} contribute notably to the bands near the Γ- and *H*-points, and along the *H*–*A* paths around E_F. Particularly, the La d_{xy} orbital takes part in the B-π hole pocket around *H*, while most of the La-f bands move from 2 to 5 eV above the Fermi level (Fig. 1(e)) with nontrivial hybridizations with the B-σ hole pocket around *A* near E_F.

The above mentioned electronic bands form three Fermi surfaces as illustrated in Fig. 1(f)–(h). They are respectively the small hole pockets around *A* constructed mainly by the B-σ orbital with partially the La-f orbital, the paraboloid hole pockets around *H* mostly comprised by the B-π with some La d_{xy}, and the star-shaped cylinder Fermi surface surrounding Γ composed of the La d orbitals. With the above band character analysis, we have adopted the sp^2, p_z orbital of B atoms and d_{z^2}, $d_{x^2-y^2}$, d_{xy}, f orbital of La atoms as the Wannier basis to build the tight-binding Hamiltonian and generate the Wannier band

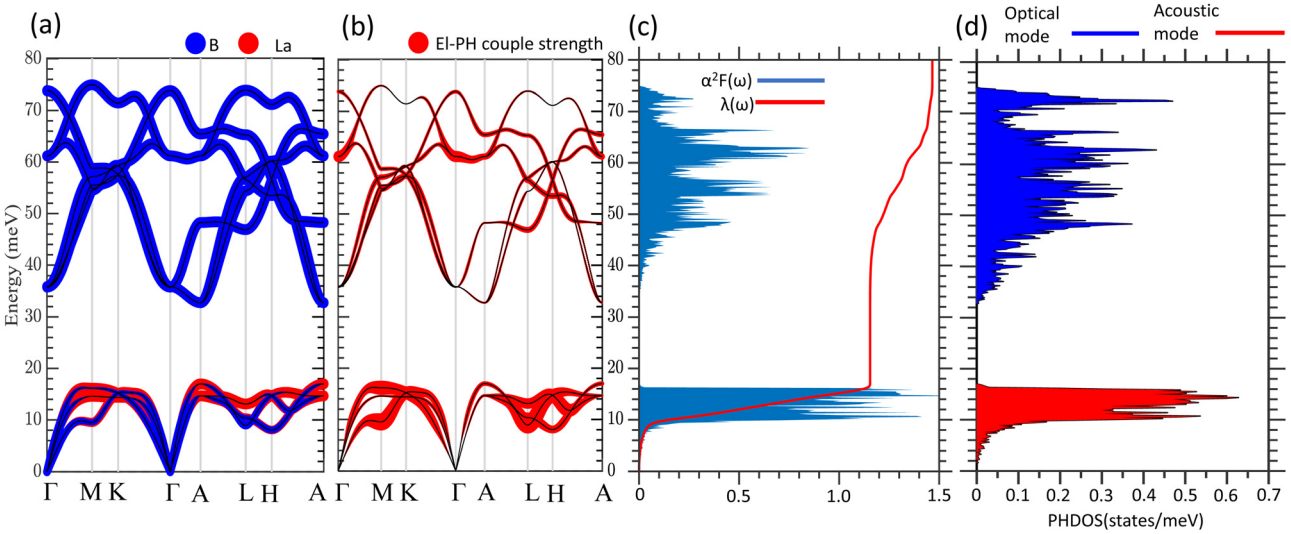

Fig. 2 LaB_2 phonon related properties. (a) Phonon dispersion with atom resolved contributions. The size of the colored spheres illustrate the atomic contributions. (b) Phonon dispersion with EPC strength λ_{qv} indicated by the size of red spheres. (c) Eliashberg function $\alpha^2F(\omega)$ and integrated Eliashberg function $\lambda(\omega)$. (d) Phonon density of states (PHDOS).

structure using Wannier90 code. This Wannier basis set can well reproduce the DFT band structures from −10 eV to 2 eV with high quality, and is used for the topological analysis as will be discussed later.

The superconductivity of LaB_2 is explored through the phonon dispersion and electron–phonon coupling (EPC) calculations based on density function perturbation theory (DFPT). Fig. 2(a) shows the phonon band structures with the atomic contributions resolved. The acoustic phonon modes in the low frequency region less than 16 meV are mainly derived from the vibrations of heavy La atoms coupled with light B atoms, while the light B atoms oscillate quickly and dominate the high frequency region above 32 meV. In between, there is a notable phonon band gap, indicating a low scattering rate between acoustic and optical phonons. The phonon density of states (DOSs) depicted in Fig. 2(d) shows the overall narrow bandwidth with high intensity for acoustic phonon bands, and wide bandwidth with low intensity for optical phonon bands. Fig. 2(b) shows the phonon-dependent EPC strength λ_{qv} of LaB_2. For the acoustic branches, there exist three Kohn anomalies around the M, L, and H points with the phonon energy significantly lowered to ∼10 meV. These three Kohn anomalies are associated with strong EPC strengths up to λ_M = 1.68, λ_L = 2.01, and λ_H = 0.6, respectively. For the optical branches, the phonon modes (point group E_{2g}) with significant EPC locate at ∼60 meV from Γ- to A-point. The maximum EPC strength λ_q = 0.46 here is much smaller than that of the Kohn anomalies in the acoustic branches. The Eliashberg spectral function presented in Fig. 2(c) demonstrates a strong peak from 10 to 16 meV with the Kohn anomalies dominating the lower part and with the relatively flat phonon bands dominating the higher part of the acoustic phonon bands. This strong acoustic phonon Eliashberg spectral function is closely related to the heavy atom La as can be seen from the atom-resolved phonon band structure in Fig. 2(a). As for the optical phonon modes, the Eliashberg spectral function is generally smaller than the acoustic counterparts. The integrated Eliashberg function over the low-frequency acoustic modes $\lambda_A(\omega)$ = 1.15 (Fig. 2(c)) is relatively strong because the Eliashberg spectral function is divided by the phonon frequency in the integral of eqn (5). Owing to the same reason, the integrated Eliashberg function over the high-frequency optical modes $\lambda_O(\omega)$ = 0.32 is lower than the acoustic counterpart, despite the wider bandwidth. Furthermore, the total EPC strength λ = 1.47 is calculated by integrating the Eliashberg spectral function over all phonon modes, in which the acoustic phonons contribute nearly 80% of the total λ.

To explore possible anisotropy and multigap superconductivity in LaB_2, we further solve the anisotropic Migdal–Eliashberg equations and analyze the contributions and anisotropic properties of EPC strength λ_{nk} for the electronic states forming the Fermi surfaces as depicted in Fig. 3. Because it has the same crystal structure as MgB_2, the Fermi surface (FS) of LaB_2 is similar to that of MgB_2 as can be seen in Fig. 3(a and b). The pipe-like FS forms a honeycomb-shape 2-dimensional network over the k_x–k_y plane with small Fermi pockets located within the honeycomb holes. Fig. 3(c and d) show that the strongest EPC (red) is distributed around the hexagon corners of the honeycomb network at the H-point. While the second strongest EPC (yellow and orange) distributes over the small Fermi pockets around the Γ- and A-points. The other regions over FS (green) show weak EPC strength only. These EPC maps demonstrate two distinct EPC features: the strongest red and the 2nd strongest yellow/orange regions depending on the k-points and the comprised atomic orbitals, evidencing the multigap superconductivity in LaB_2.

The corresponding EPC-induced superconducting gaps in the Fermi surfaces over the BZ are presented in Fig. 3(e and f). Good correspondence with the EPC maps in Fig. 3(c and d) can be clearly seen, showing that the electronic states on the Fermi

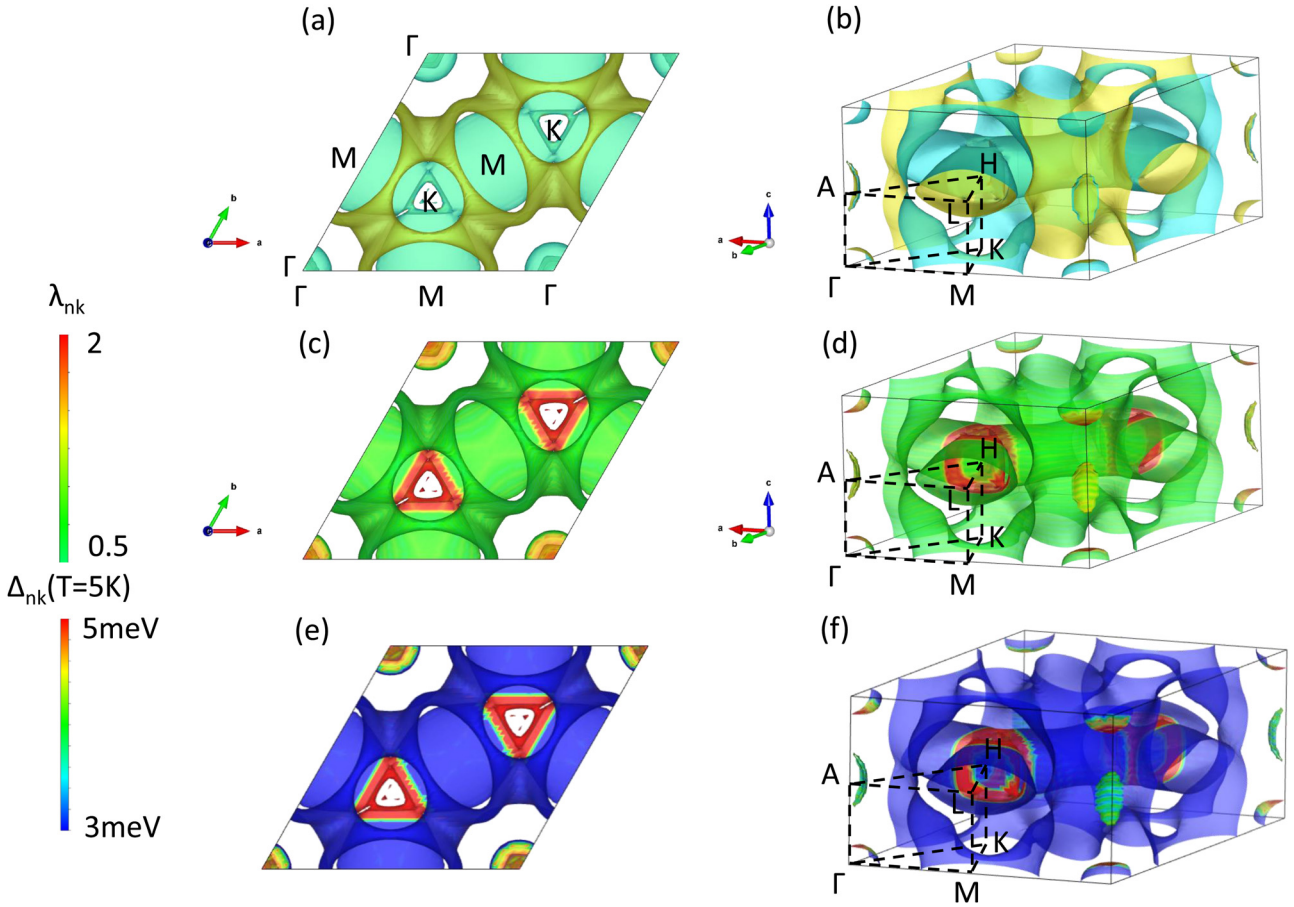

Fig. 3 EPC distribution on Fermi surface and contributions to superconducting gaps of LaB_2. (a) Top and (b) side view of the Fermi surface (FS) in the primitive *BZ*. Dash lines in (b) show the high symmetry lines in *BZ*. (c) Top and (d) side view of the momentum-resolved EPC at FS. The red color region around k_z = 0.4 KH indicates the maxima EPC region. (e) Top and (f) side view of the momentum-resolved superconductivity gap at T = 5 K. The red color region around k_z = 0.4 KH indicates the maximum SC gap region.

surface with higher EPC contribute strongly to the superconducting gaps. Overall, one can see two main features in the superconducting gap distributions: (I) the large gap ($\Delta_{nk} \simeq 5$ meV) regions around the zone center and *H*-point at $k_z \simeq 0.4$ indicated by red color; (II) the middle gap ($\Delta_{nk} \simeq 4$ meV) areas denoted by yellow and orange colors around Γ and A points. Combining these two main features in the superconducting-gap maps (Fig. 3(e and f)) with the strongest and second strongest EPC distributions (Fig. 3(c and d)), we demonstrate clearly the two-gap superconductivity in LaB_2 similar to MgB_2.

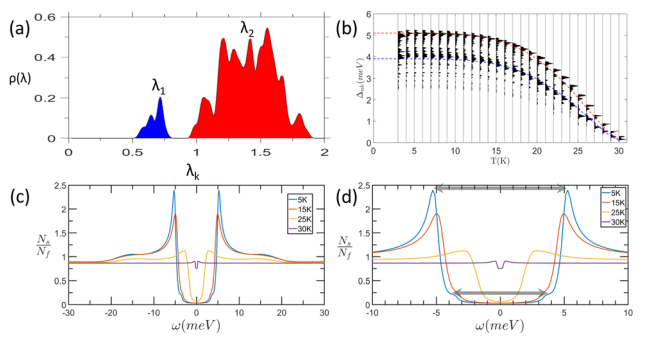

Fig. 4 EPC strength distribution, superconducting gap and DOS of LaB_2 (a) EPC distribution ρ_{nk} as a function of the EPC strength λ_{nk}. (b) Superconductivity gap distribution at the Fermi surface from T = 3 K to T = 30 K. Blue and red dash curves are obtained from fitting the superconductivity gap equation using the maximum gap distribution. (c) Quasiparticle density of states at T = 5 K, 15 K, 25 K, 30 K (blue, red, yellow, and purple curves, respectively). (d) Zoom in plot of (c). Gray arrows indicate the 2 gaps.

To quantify the EPC distribution over the *BZ* presented in Fig. 3(c and d), the EPC distribution ρ_{nk} as a function of the EPC strength λ_{nk} is integrated through

$$\rho(\lambda) = \sum_n \int \frac{d^3k}{\Omega_{BZ}} \delta(\lambda - \lambda_{nk}) \delta(\varepsilon_{nk} - E_F), \quad (1)$$

and is depicted in Fig. 4(a). It can be seen clearly that there exist two distinct peaks at $\lambda_1 \sim 0.75$ and $\lambda_2 \sim 1.5$. The former is a low-intensity peak with a narrow width while the latter is a high-intensity peak with a wide width. According to the orbital character analysis based on Fig. 1(c–e) and 3(c, d), the weak λ_1 peak is mainly composed of the B-σ band (*A*-point) as well as the B-π and La-d_{z^2} hybridized band (Γ-point) along the Γ–*A*–Γ *k*-path crossing the Fermi level. These two bands (B-σ and B-π La-d_{z^2} hybridized band) contribute equally to the EPC λ_1 with

the same gap (Fig. 3(e, f) and 4(b)). This is the reason why we observe only two EPC peaks in Fig. 4(a) even though we see three bands (FSs) in Fig. 1(c–h). As for the strong λ_2 peak, the main contribution is comprised of the B-π band hybridizing with two La-d orbitals ($d_{x^2-y^2}$ and d_{xy}) (Fig. 1(c–e)) around the *H*-point along the *L–H–A* *k*-path crossing the Fermi level, which shows a very strong EPC nature. Different from MgB_2, the EPC strengths of these B-π La-d hybridized bands is much stronger than that of the B-σ bond in LaB_2. The strongly enhanced EPC of the B-π bond by hybridization with La-d orbitals demonstrates the potential of d-orbitals in superconductivity.

Fig. 4(b) shows the calculated superconductivity gap energy distribution *versus* temperature from 3 to 30 K. Overall, the two-gap features can be clearly seen. Close to the zero temperature limit, the two gap values are ∼3.9 and ∼5.1 meV for Δ_1 and Δ_2, respectively. While above T = 20 K, both the gap values decrease to zero. By using the BCS-like gap equation non-linear fit for the calculated superconducting gap functions, we obtain two curves for Δ_1 and Δ_2 as functions of temperature. The two gap curves converge to 0 at T = 30 K. Fig. 4(c and d) shows the superconductivity density of states at T = 5, 15, 25, 30 K. At T = 5 K, one can clearly see the two peaks at ±3.9 meV and ±5.1 meV. At T = 30 K, both the high and low energy SC gaps are nearly vanishing owing to the approaching superconducting transition temperature. Based on our fitting gap functions in Fig. 4(b) and superconductivity DOS in Fig. 4(c) and (d), we conclude the two-gap superconducting T_c = 30 K.

Another important research area in borophene–metal systems is topological superconduction. The Dirac nodal line and topological surface state have been discovered in MgB_2 owing to the spatial inversion symmetry and time-reversal symmetry (PT symmetry).[37] MgB_2 is topologically nontrivial not only electronically, but also phononically. The phononic Weyl nodal line and phononic surface arc states have been reported in MgB_2.[38] In addition, with Mg being replaced by other metal atoms, TiB_2 and ZrB_2 have also been theoretically reported to show PT symmetry protected electronic Dirac nodal lines.[39] The topological surface state and Dirac nodal line in ZrB_2 have further been detected by angle-resolved photoemission spectroscopy (ARPES).[40] On the one hand, these interesting electronic topological results are cornerstones for hosting Majorana fermions. On the other hand, the phononic topological results can support phonon-related phenomena such as electrical resistance, heat conduction, and phonon waveguides.[38]

To explore the topological properties in LaB_2, we performed topological calculations including the Wilson loop, topological index, inverted band structure, Greens function, and surface states. Here we demonstrate the main conclusion in the topological aspect given from the Wilson loop calculations for the topological index $\mathbb{Z}_2$. The other calculated results are presented in the ESI.† As can be seen in Fig. 5(a)–(d), the Berry phase of the Wannier center shows even winding numbers along k_x and k_y in *BZ*. On the contrary, the corresponding winding numbers are odd in both the k_z = 0 and k_z = 0.5 planes (see red lines and numbers in Fig. 5(e) and (f)). Consequently, LaB_2 belongs to the weak topological insulator category[41,42] with the $\mathbb{Z}_2$ index

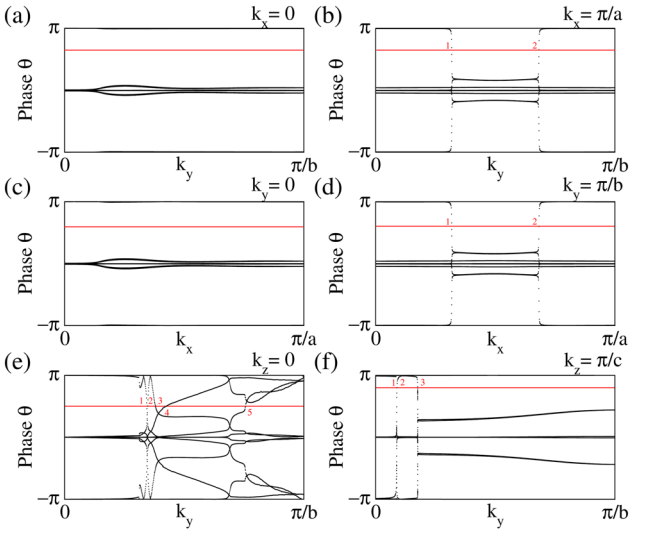

Fig. 5 Wannier charge center (WCC) evolution (Wilson loop) in three-axis planes of *BZ* for time-reversal invariant LaB_2. (a) $\mathbb{Z}_2 = 0$ for k_x = 0.0. (b) $\mathbb{Z}_2 = 0$ for k_x = π/*a*. (c) $\mathbb{Z}_2 = 0$ for k_y = 0.0. (f) $\mathbb{Z}_2 = 0$ for k_y = π/*b*. (e) $\mathbb{Z}_2 = 1$ for k_z = 0.0 (b) $\mathbb{Z}_2 = 1$ for k_z = π/*c*. The solid red line is the reference line for determining the $\mathbb{Z}_2$ topological invariance. Combining all together leads to the weak topological insulator state for LaB_2.

$\mathbb{Z}_2 = (0; 001)$. This $\mathbb{Z}_2$ index also implies that except for the (0001) surface, the topological surface states exist in the other surfaces of LaB_2. Detailed topological surface states of LaB_2 can be found in the ESI.† Moreover, this topological index could be tuned from a weak to strong topological insulator by applying strain or doping, as will be discussed later.

To date, the superconducting T_c of the available topological superconductors such as $PbTaSe_2$,[43,44] PdBi,[45,46] $RhPb_2$,[47] and WS_2[48] are all below 10 K. Such low superconducting temperatures cause tremendous difficulties for accurately measuring the possible Majorana fermions experimentally.[43,49] Thus our predicted high-T_c of 30 K in topological superconductor LaB_2 is of great importance. By applying external pressures and doping levels, we carry out the three-phase diagram calculations and present the results in Fig. 6. The superconducting temperature calculated using the Allen–Dynes modified McMillan formula varies from ∼15 K to ∼30 K, indicating T_c can be further enhanced under certain conditions. Besides, the topological behavior analyzed by the $\mathbb{Z}_2$ topological numbers is also tunable from weak to strong topology. Both the tunable T_c and topology demonstrate that LaB_2 is a rarely found convincing candidate in the topological superconductor research field.

Conclusion

In summary, we have shown that LaB_2 is a three-band two-gap topological superconductor with T_c^{aniso} = 30 K by using DFPT calculations and solving the fully anisotropic Migdal–Eliashberg equations. First-principles DFPT calculations show that LaB_2 is dynamically stable with $T_c^{McMillan}$ = 22 K from the Allen–Dynes modified McMillan formula. By including the anisotropic effect in the Migdal–Eliashberg equations, the T_c^{aniso} of LaB_2

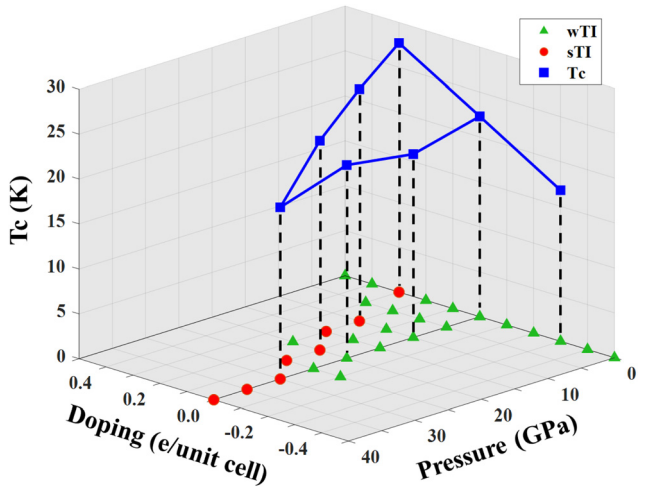

Fig. 6 Three-phase diagram of topological superconductor LaB_2 under various pressures and doping levels. Red dots and green triangles denote strong and weak topological insulators, respectively. Blue squares indicate the superconducting temperatures of LaB_2 calculated using the Allen–Dynes modified McMillan formula with the doping and pressure conditions indicated by the black dotted lines. Tunable T_c ranging from ~15 K to ~30 K and topological phases from weak to strong topological insulator are shown.

can be significantly raised up to 30 K. The calculated SC gap $\Delta_\sigma(T = 0\ \text{K})$ and $\Delta_\pi(T = 0\ \text{K})$ are 5.1 meV and 3.9 meV, respectively. In comparison with MgB_2, the enhanced λ in LaB_2 is most likely due to the hybridization between the La-d orbitals and borophene π bonds. The topological index $\mathbb{Z}_2 = (0;001)$ indicates that LaB_2 belongs to the weak TI category. We suggest to adopt the d orbitals as an extra factor to enhance the electron–phonon coupling strength for multigap superconductors. Furthermore, we also show that under given pressure and doping conditions, the topology and T_c in LaB_2 are both tunable from weak to strong and from ~15 K to ~30 K, respectively. Our work thus paves a new platform for manipulating topological superconductors.

Methods

Electronic property calculations are performed using the Vienna *ab initio* simulation package (VASP)[50–53] adopting the projector-augmented plane wave (PAW)[54,55] pseudopotential with the Perdew–Burke–Ernzerhof (PBE)[64] functional based on density functional theory (DFT). A *k*-mesh of 18 × 18 × 18 and kinetic energy cutoff of 400 eV are adopted in the electronic calculations. *Ab initio* phonon calculations are preformed using the Quantum Espresso code[56] based on density functional theory (DFT). Pseudopotentials with the Perdew–Burke–Ernzerhof (PBE) exchange–correlation functional are generated by the Optimized Norm-Conserving Vanderbilt Pseudopotential (ONCVPSP) code.[57] The plane wave basis with the cutoff kinetic energy of 80 Ry are used. 24 × 24 × 24 *k*-mesh and 6 × 6 × 6 *q*-mesh with Methfessel–Paxton smearing of 0.04 Ry[58] are adopted in the self-consistent electron and phonon calculations based on density function perturbation theory (DFPT). Superconducting critical temperatures T_c are calculated not only by using the Allen–Dynes modified McMillan formula[59] in eqn (2)–(5) but also by solving the anisotropic Migdal–Eliashberg equations on the imaginary-axis[20] in eqn (6) and (7).

$$T_c = \frac{\omega_{ln}}{1.20}\exp\left(\frac{-1.04(1+\lambda)}{\lambda-\mu_c^*(1+0.62\lambda)}\right) \quad (2)$$

The logarithmic average phonon frequency ω_{ln} and the Eliashberg function α^2F are

$$\omega_{ln} = \exp\left(\frac{2}{\lambda}\int d\omega \frac{\ln\omega}{\omega}\alpha^2F(\omega)\right) \quad (3)$$

$$\alpha^2F = \frac{1}{2}\int_{BZ} dq\lambda_{q\nu}\omega_{q\nu}\delta(\omega-\omega_{q\nu}) \quad (4)$$

The contribution of electron–phonon coupling from different phonon frequencies, the $\lambda(\omega)$ is calculated through

$$\lambda(\omega) = \int_0^\omega \sum_{q\nu}^0 \lambda_{q\nu}(\omega')d\omega' = \int \frac{2\alpha^2F}{\omega'}d\omega' \quad (5)$$

$$Z_{nk}(i\omega_j) = 1 + \frac{\pi T}{\omega_j N_F}\sum_{mj'}\int\frac{d^3q}{\Omega_{BZ}}\frac{\omega_{j'}}{\sqrt{\omega_{j'}^2+\Delta_{mk+q}{}^2(i\omega_{j'})}} \times \lambda_{nk,mk+q}(\omega_j-\omega_{j'})\delta(\varepsilon_{nk}) \quad (6)$$

$$Z_{nk}(i\omega_j)\Delta_{nk}(i\omega_j) = \frac{\pi T}{N_F}\sum_{mj'}\int\frac{d^3q}{\Omega_{BZ}}\frac{\omega_{j'}}{\sqrt{\omega_{j'}^2+\Delta_{mk+q}{}^2(i\omega_{j'})}} \times [\lambda_{nk,mk+q}(\omega_j-\omega_{j'})-\mu_c^*]\delta(\varepsilon_{nk}). \quad (7)$$

To solve the anisotropic Migdal–Eliashberg equations, the EPW (electron–phonon Wannier, electron–phonon coupling using Wannier function)[20,60,61] and Wannier90[62] codes are utilized. The sp^2, p_z orbitals of B atoms and d_{z^2}, $d_{x^2-y^2}$, d_{xy}, f orbitals of La atom are included in the projection of the Wannier basis with a uniform 12 × 12 × 12 *k*-mesh. Furthermore, for the EPC interpolation, a *k*-grid of 60 × 60 × 60 and *q*-grid of 30 × 30 × 30 are used. Matsubara frequencies for fermions, $i\omega_j = (2j+1)\pi T$, are set with a cutoff energy of 0.3 eV greater than four times of the maximum phonon energy. The effective Coulomb potential $\mu_c^* = 0.1$ eV and convergence threshold less 10^{-4} eV are used in solving the Eliashberg equations. To study topological properties, iterative surface Green's function and Wilson loop simulations are carried out *via* the WannierTools package[63] with the same tight-binding Wannier Hamiltonian.

Data availability

The data that support the findings of this study are available from the authors upon reasonable request.

Author contributions

H. T. J. conceived the project. C. H. C. and Y. S. L. carried out the DFPT calculations and topological analysis, respectively. A. H. supervised the calculations. All authors contributed to discussions and the final manuscript.

Conflicts of interest

The authors declare no competing financial or non-financial interests.

Acknowledgements

This work was supported by the Ministry of Science and Technology, Taiwan. H.-T. J. also thanks support from NCHC, CINC-NTU, AS-iMATE-109-13, and CQT-NTHU-MOE, Taiwan.

References

1 A. P. Drozdov, M. I. Eremets, I. A. Troyan, V. Ksenofontov and S. I. Shylin, *Nature*, 2015, **525**, 73.
2 A. P. Drozdov, P. P. Kong, V. S. Minkov, S. P. Besedin, M. A. Kuzovnikov, S. Mozaffari, L. Balicas, F. F. Balakirev, D. E. Graf and V. B. Prakapenka, *et al.*, *Nature*, 2019, **569**, 528.
3 A. M. Shipley, M. J. Hutcheon, R. J. Needs and C. J. Pickard, *Phys. Rev. B*, 2021, **104**, 054501, DOI: 10.1103/PhysRevB.104.054501.
4 C.-H. Chen, A. Huang, C. C. Tsuei and H.-T. Jeng, *New J. Phys.*, 2021, **23**, 093007.
5 J. Nagamatsu, N. Nakagawa, T. Muranaka, Y. Zenitani and J. Akimitsu, *Nature*, 2001, **410**, 63.
6 H. J. Choi, D. Roundy, H. Sun, M. L. Cohen and S. G. Louie, *Phys. Rev. B: Solid State*, 2002, **66**, 020513.
7 K. Jin, N. P. Butch, K. Kirshenbaum, J. Paglione and R. L. Greene, *Nature*, 2011, **476**, 73.
8 P. A. Lee, N. Nagaosa and X.-G. Wen, *Rev. Mod. Phys.*, 2006, **78**, 17, DOI: 10.1103/RevModPhys.78.17.
9 J. P. Carbotte, E. Schachinger and D. N. Basov, *Nature*, 1999, **401**, 354.
10 T. Dahm, *et al.*, *Nat. Phys.*, 2009, **5**, 217.
11 D. H. Lu, M. Yi, S.-K. Mo, A. S. Erickson, J. Analytis, J.-H. Chu, D. J. Singh, Z. Hussain, T. H. Geballe and I. R. Fisher, *et al.*, *Nature*, 2008, **455**, 81.
12 F. Wang and D.-H. Lee, *Science*, 2011, **332**, 200.
13 C. Kallin, *Rep. Prog. Phys.*, 2012, **75**, 042501.
14 J. M. An and W. E. Pickett, *Phys. Rev. Lett.*, 2001, **86**, 4366.
15 J. Kortus, I. I. Mazin, K. D. Belashchenko, V. P. Antropov and L. L. Boyer, *Phys. Rev. Lett.*, 2001, **86**, 4656.
16 K.-P. Bohnen, R. Heid and B. Renker, *Phys. Rev. Lett.*, 2001, **86**, 5771.
17 T. Yildirim, O. Gulseren, J. W. Lynn, C. M. Brown, T. J. Udovic, Q. Huang, N. Rogado, K. A. Regan, M. A. Hayward and J. S. Slusky, *et al.*, *Phys. Rev. Lett.*, 2001, **87**, 037001.
18 Y. Kong, O. V. Dolgov, O. Jepsen and O. K. Andersen, *Phys. Rev. B: Condens. Matter Mater. Phys.*, 2001, **64**, 020501.
19 H. J. Choi, D. Roundy, H. Sun, M. L. Cohen and S. G. Louie, *Nature*, 2002, **418**, 758.
20 E. R. Margine and F. Giustino, *Phys. Rev. B: Condens. Matter Mater. Phys.*, 2013, **87**, 024505.
21 M. Iavarone, G. Karapetrov, A. E. Koshelev, W. K. Kwok, G. W. Crabtree, D. G. Hinks, W. N. Kang, E.-M. Choi, H. J. Kim and H.-J. Kim, *et al.*, *Phys. Rev. Lett.*, 2002, **89**, 187002.
22 P. Szabo, P. Samuely, J. Kacmarcik, T. Klein, J. Marcus, D. Fruchart, S. Miraglia, C. Marcenat and A. G. M. Jansen, *Phys. Rev. Lett.*, 2001, **87**, 137005.
23 R. S. Gonnelli, D. Daghero, G. A. Ummarino, V. A. Stepanov, J. Jun, S. M. Kazakov and J. Karpinski, *Phys. Rev. Lett.*, 2002, **89**, 247004.
24 R. M. da Silva, M. V. Miloševic, A. A. Shanenko, F. M. Peeters and J. A. Aguiar, *Sci. Rep.*, 2015, **5**, 1.
25 J. Garaud, J. Carlstrm and E. Babaev, *Phys. Rev. Lett.*, 2011, **107**, 197001.
26 E. Babaev, *Phys. Rev. Lett.*, 2002, **89**, 067001.
27 L. Komendov, Y. Chen, A. A. Shanenko, M. V. Miloševic and F. M. Peeters, *Phys. Rev. Lett.*, 2012, **108**, 207002.
28 M. Silaev and E. Babaev, *Phys. Rev. B: Condens. Matter Mater. Phys.*, 2012, **85**, 134514.
29 N. V. Orlova, A. A. Shanenko, M. V. Miloševic, F. M. Peeters, A. V. Vagov and V. M. Axt, *Phys. Rev. B: Condens. Matter Mater. Phys.*, 2013, **87**, 134510.
30 V. Stanev and Z. Tešanović, *Phys. Rev. B: Condens. Matter Mater. Phys.*, 2010, **81**, 134522.
31 J. Bekaert, A. Aperis, B. Partoens, P. M. Oppeneer and M. V. Miloševic, *Phys. Rev. B*, 2017, **96**, 094510.
32 C. Sevik, J. Bekaert, M. Petrov and M. V. Milošević, *Phys. Rev. Mater.*, 2022, **6**, 024803, DOI: 10.1103/PhysRevMaterials.6.024803.
33 Y. Zhao, C. Lian, S. Zeng, Z. Dai, S. Meng and J. Ni, *Phys. Rev. B*, 2020, **101**, 104507.
34 H. Rosner, A. Kitaigorodsky and W. E. Pickett, *Phys. Rev. Lett.*, 2002, **88**, 127001.
35 Y. Zhao, C. Lian, S. Zeng, Z. Dai, S. Meng and J. Ni, *Phys. Rev. B*, 2019, **100**, 094516.
36 S. Souma, Y. Machida, T. Sato, T. Takahashi, H. Matsui, S.-C. Wang, H. Ding, A. Kaminski, J. C. Campuzano and S. Sasaki, *et al.*, *Nature*, 2003, **423**, 65.
37 K.-H. Jin, H. Huang, J.-W. Mei, Z. Liu, L.-K. Lim and F. Liu, *npj Comput. Mater.*, 2019, **5**, 1.
38 J. Li, Q. Xie, J. Liu, R. Li, M. Liu, L. Wang, D. Li, Y. Li and X.-Q. Chen, *Phys. Rev. B*, 2020, **101**, 024301.
39 X. Feng, C. Yue, Z. Song, Q. Wu and B. Wen, *Phys. Rev. Mater.*, 2018, **2**, 014202.
40 R. Lou, P. Guo, M. Li, Q. Wang, Z. Liu, S. Sun, C. Li, X. Wu, Z. Wang and Z. Sun, *et al.*, *npj Quantum Mater.*, 2018, **3**, 1.
41 L. Fu, C. L. Kane and E. J. Mele, *Phys. Rev. Lett.*, 2007, **98**, 106803.
42 R. Yu, X. L. Qi, A. Bernevig, Z. Fang and X. Dai, *Phys. Rev. B: Condens. Matter Mater. Phys.*, 2011, **84**, 075119.
43 S.-Y. Guan, P.-J. Chen, M.-W. Chu, R. Sankar, F. Chou, H.-T. Jeng, C.-S. Chang and T.-M. Chuang, *Sci. Adv.*, 2016, **2**, e1600894.

44 T.-R. Chang, P.-J. Chen, G. Bian, S.-M. Huang, H. Zheng, T. Neupert, R. Sankar, S.-Y. Xu, I. Belopolski and G. Chang, *et al.*, *Phys. Rev. B*, 2016, **93**, 245130.
45 P. K. Biswas, D. G. Mazzone, R. Sibille, E. Pomjakushina, K. Conder, H. Luetkens, C. Baines, J. L. Gavilano, M. Kenzelmann and A. Amato, *et al.*, *Phys. Rev. B*, 2016, **93**, 220504.
46 K. Dimitri, M. M. Hosen, G. Dhakal, H. Choi, F. Kabir, C. Sims, D. Kaczorowski, T. Durakiewicz, J.-X. Zhu and M. Neupane, *Phys. Rev. B*, 2018, **97**, 144514.
47 J.-F. Zhang, P.-J. Guo, M. Gao, K. Liu and Z.-Y. Lu, *Phys. Rev. B*, 2019, **99**, 045110.
48 Y. Fang, J. Pan, D. Zhang, D. Wang, H. T. Hirose, T. Terashima, S. Uji, Y. Yuan, W. Li and Z. Tian, *et al.*, *Adv. Mater.*, 2019, **31**, 1901942.
49 G. Bian, T.-R. Chang, R. Sankar, S.-Y. Xu, H. Zheng, T. Neupert, C.-K. Chiu, S.-M. Huang, G. Chang and I. Belopolski, *et al.*, *Nat. Commun.*, 2016, **7**, 1.
50 G. Kresse and J. Hafner, *Phys. Rev. B: Condens. Matter Mater. Phys.*, 1993, **47**, 558.
51 G. Kresse and J. Hafner, *Phys. Rev. B: Condens. Matter Mater. Phys.*, 1994, **49**, 14251.
52 G. Kresse and J. Furthmüller, *Comput. Mater. Sci.*, 1996, **6**, 15.
53 G. Kresse and J. Furthmüller, *Phys. Rev. B: Condens. Matter Mater. Phys.*, 1996, **54**, 11169.
54 P. E. Blöchl, *Phys. Rev. B: Condens. Matter Mater. Phys.*, 1994, **50**, 17953.
55 G. Kresse and D. Joubert, *Phys. Rev. B: Condens. Matter Mater. Phys.*, 1999, **59**, 1758.
56 P. Giannozzi, S. Baroni, N. Bonini, M. Calandra, R. Car, C. Cavazzoni, D. Ceresoli, G. L. Chiarotti, M. Cococcioni and I. Dabo, *et al.*, *J. Phys.: Condens. Matter*, 2009, **21**, 395502.
57 D. R. Hamann, *Phys. Rev. B: Condens. Matter Mater. Phys.*, 2013, **88**, 085117.
58 M. Methfessel and A. T. Paxton, *Phys. Rev. B: Condens. Matter Mater. Phys.*, 1989, **40**, 3616.
59 P. B. Allen and R. C. Dynes, *Phys. Rev. B: Solid State*, 1975, **12**, 905.
60 S. Poncé, E. Margine, C. Verdi and F. Giustino, *Comput. Phys. Commun.*, 2016, **209**, 116.
61 F. Giustino, M. L. Cohen and S. G. Louie, *Phys. Rev. B: Condens. Matter Mater. Phys.*, 2007, **76**, 165108.
62 G. Pizzi, V. Vitale, R. Arita, S. Blügel, F. Freimuth, G. Géranton, M. Gibertini, D. Gresch, C. Johnson and T. Koretsune, *et al.*, *J. Phys.: Condens. Matter*, 2020, **32**, 165902.
63 Q. Wu, S. Zhang, H.-F. Song, M. Troyer and A. A. Soluyanov, *Comput. Phys. Commun.*, 2018, **224**, 405.
64 J. P. Perdew, K. Burke and M. Ernzerhof, *Phys. Rev. Lett.*, 1996, **77**, 3865.